Synthesis and Characterization of Pt−WO_3 as Methanol Oxidation Catalysts for Fuel Cells

Shrisudersan Jayaraman,[†] Thomas F. Jaramillo,[†] Sung-Hyeon Baeck,[‡] and Eric W. McFarland*,[†]

Mitsubishi Chemical Center for Advanced Materials and Department of Chemical Engineering, University of California, Santa Barbara, California 93106, and Department of Chemical Engineering, Inha University, Incheon 402-751, South Korea

Received: June 8, 2005; In Final Form: September 7, 2005

Several compositions of Pt−WO_3 catalysts were synthesized and characterized for the electro-oxidation of methanol and CO. The surface morphologies of the catalysts were found to be dependent on the composition. X-ray energy dispersive spectroscopy and X-ray photoelectron spectroscopy results suggest a surface enrichment of WO_3 in the codeposited Pt−WO_3 catalysts. Cyclic voltammetry and chronoamperometry in methanol show an improvement in catalytic activity for the Pt−WO_3 catalysts. A significant improvement in the poison tolerance toward CO and other organic intermediates was observed in the mixed metal−metal oxide catalyst. The catalytic performance of the different compositons was directly compared by normalization of the current to active sites. CO-stripping voltammetry suggests the involvement of WO_3 in the catalytic process as opposed to a mere physical effect as suggested by previous work. A possible mechanism for this improvement is proposed based on the electrochemical data.

Introduction

Direct methanol fuel cells (DMFCs) are being widely studied for compact, high-power-density energy conversion.[1−6] Methanol has a low theoretical oxidation potential ($E^\circ = 0.03$ V) comparable to that of hydrogen ($E^\circ = 0$ V), and in principle it can be used as an efficient fuel in low-temperature polymer electrolyte membrane fuel cells. Methanol possesses practical advantages over hydrogen as a fuel since it is a liquid at room temperature and pressure and requires no preprocessing modules such as reformers. Despite these advantages, high overpotentials for the methanol oxidation reaction prevent the use of DMFCs in practical applications. This is due to the presence of partial oxidation intermediates such as $-CH_3O$, $-CH_2O$, $-CHO$, and $-CO$, which adsorb strongly on the surface of the best known cost-effective catalysts resulting in deactivation.

Several studies have been performed on Pt-based multicomponent catalysts to improve the poison tolerance with the ultimate goal of creating cost-effective catalysts in practical fuel cells. Metals including ruthenium, osmium, iridium, rhodium, tin, etc. have been shown to improve the catalytic activity of Pt either by modifying the electronic properties of Pt or by modifying the surface chemistry to produce a bifunctional material.[7−16] In the bifunctional mechanism, the alloyed metal forms surface oxides at potentials much lower than on Pt, which provides local oxygen to oxidize the poisons to desorbing products. In the electronic effect (or the ligand effect), the alloyed metal modifies the electronic structure of Pt, resulting in a lower bond strength of the adsorbed species on Pt. Although these multicomponent catalysts have demonstrated superior performance to Pt, they remain prohibitively expensive for use in portable consumer applications since the alloyed metals are as scarce or more scarce than Pt.

Metal−metal oxide catalysts are also being investigated for electro-oxidation reactions. Specifically, tungsten oxide (WO_3)-based catalysts have been studied by several groups as potential low-cost fuel cell catalysts.[17−25] Studies on a limited number of Pt−WO_3 compositions are reported, and the improvement in catalytic activity is attributed to physical effects (such as increase in surface area) rather than any catalytic effects of WO_3.

In this paper, we report the investigations of a wide range of compositions of Pt−WO_3 (0−100% Pt) for the electro-oxidation of methanol and their implications toward DMFCs. The catalysts were prepared by an electrochemical route, and systematic physical and electrochemical characterization was performed. Specifically the following questions were addressed: (1) Does support of Pt on WO_3 increase the CO tolerance of Pt-based fuel cell catalysts? (2) What is the specific role of the WO_3 and the mechanism for the observed poison tolerance? (3) Is there an optimum ratio of Pt/WO_3? (4) Are both the catalytic activity and the utilization of Pt improved? (5) What is the best means for determining the electrochemically active surface area?

Experimental Methods

Substrates. The supported Pt−WO_3 catalysts were synthesized on fluorine-doped tin oxide (FTO) substrates (Tec 8, 2.3-mm-thick glass, Hartford Glass Co., Hartford City, IN) cut into 2.5 cm × 1.25 cm sections. Prior to deposition, the substrates were sonicated in a 50:50 ethanol−water mixture for 15 min followed by thorough rinsing in deionized (DI) water, sonication in DI water, and drying in a stream of nitrogen.

Electrolytes. An aqueous solution of chloroplatinic acid (H_2PtCl_6, Aldrich) was used as the source of Pt^{4+} ions in the deposition solution. Preparation of the tungsten peroxo electrolyte used in the deposition of WO_3 is described elsewhere.[18] Briefly, 1.84 g of tungsten powder (Aldrich) was dissolved in 60 mL of 30% hydrogen peroxide solution by stirring for ∼5 h followed by the decomposition of excess peroxide with Pt black. The solution was diluted to 50 mM using a 50:50 mixture of

* Author to whom correspondence should be addressed. Phone: (805) 893-4343. Fax: (805) 893-4731. E-mail: mcfar@engineering.ucsb.edu.
[†] University of California, Santa Barbara.
[‡] Inha University.

10.1021/jp053053h CCC: $30.25
Published on Web 11/10/2005

TABLE 1: Summary of Pt−WO_3 Samples with Their Pt Surface Area (Cu−UPD)

no.	sample	% Pt^{4+} in deposition solution	Pt surface area (cm^2)
S1	Pt	100	1.0314
S2	WO_3		
S3	Pt on WO_3		0.3582
S4	Pt−WO_3	0.352	0.6283
S5	Pt−WO_3	1.960	1.0157
S6	Pt−WO_3	2.17	1.5851
S7	Pt−WO_3	7.89	2.5861
S8	Pt−WO_3	11.46	2.6818
S9	Pt−WO_3	23.08	1.5516

water and 2-propanol. The electrolytes for electrochemical characterization included sulfuric acid and methanol (Fisher Scientific) in DI water and were deaerated with N_2 (99.998%, Praxair, Santa Barbara, CA). For CO-oxidation experiments, the sulfuric acid solution was saturated with CO prior to adsorption on the catalyst surface at 0.05 V vs a reversible hydrogen electrode (RHE) and removed following adsorption by purging N_2 for 20 min at the same potential.

Electrochemical Experiments. Electrochemical experiments were performed using a potentiostat (EG&G 273A, Princeton Applied Research, Oak Ridge, TN) controlled by custom software written in LabVIEW. Potential pulses used for electrodeposition were generated by a software-triggered pulse train with a frequency of up to 40 kHz generated with a data acquisition board (DAQ) (PCI-6036E, National Instruments, Austin, TX). A platinum mesh counter electrode and an Ag/AgCl (in 4 M KCl) reference electrode were used during the electrochemical experiments. All potentials reported in this paper were converted to the RHE scale unless stated otherwise.

Scanning Electron Microscopy. Morphology and composition were characterized using a scanning electron microscope (Philips XL 30 ESEM FEG) to obtain secondary electron images as well as simultaneous electron-stimulated X-ray energy dispersive spectroscopy (EDS; PRISM IG X-ray detector, Princeton Gamma Tech, Rocky Hill, NJ) to measure the composition of the catalyst samples. The Pt Mα line at 2.048 keV and W Mα line at 1.774 keV were used for the quantitative compositional analysis. As these two lines are well-separated, the amounts of Pt and W in the samples can be determined without any interference from either of the components.

X-ray Photoelectron Spectroscopy. X-ray photoelectron spectroscopy (XPS) was employed for two purposes: first, to determine surface ratios of Pt/W for each sample, and second, to observe the valence states for both species. The XPS system (Kratos Axis Ultra) uses a monochromated Al Kα source for incident radiation and an eight-channel detector for the measurement of ejected photoelectrons. XPS measurements were taken after the samples were tested for methanol electro-oxidation. Charge compensation was utilized during measurement, and base pressure was maintained at $\leq 5.0 \times 10^{-9}$ Torr. Spectra were calibrated to the C 1s peak at 285.0 eV, arising from adventitious carbon on each sample surface. For the calculation of surface Pt/W ratios, Scofield sensitivity factors were used.[26]

Electrochemical Synthesis of Pt−WO_3 Catalysts. Nine different samples of Pt−WO_3 with compositions ranging from 0 to 100% Pt were electrochemically deposited on FTO substrates (Table 1). Sample S1 represents pure Pt electrodeposited from a solution containing 1 mM H_2PtCl_6; sample S2 is pure WO_3 electro-deposited from a 50 mM peroxo-tungsten electrolyte; sample S3 is Pt deposited onto a substrate previously deposited with WO_3 (serial deposition); samples S4−S9 consist of codeposited Pt−WO_3. For S4−S9, the relative concentration of Pt^{4+} in the solution was varied by mixing the H_2PtCl_6 and peroxo-tungsten electrolytes in different ratios.

The electrochemical deposition conditions for all the samples were identical except for the solution composition in each deposition bath. A potential pulse between 0 and −1.0 V vs Ag/AgCl was applied at a frequency of 200 Hz for 15 min. For sample S3, WO_3 was electro-deposited first on the FTO substrate for 15 min from a 50 mM peroxo-tungsten electrolyte followed by electro-deposition of Pt from a 1 mM H_2PtCl_6 solution for 10 min. All samples were rinsed thoroughly with DI water and dried under a stream of nitrogen immediately after synthesis.

Determination of Pt Surface Area. The measurement of the active surface area of the catalysts is critical for evaluating catalytic activities. The electrochemical surface area of a Pt catalyst is usually determined by the hydrogen underpotential deposition (H−UPD) method. This method is based on the fact that each surface atom of Pt adsorbs one hydrogen atom, and the charge associated with adsorption−desorption reactions provides the number of active Pt sites and the surface area.

$$Pt + H^+ + e^- \rightarrow Pt{-}H \qquad (1)$$

For a polycrystalline Pt electrode, the charge associated with the above reaction is 210 $\mu C\ cm^{-2}$.

When Pt is alloyed with metals or metal oxides, the H−UPD method fails in most cases due to the electrochemical current associated with the alloyed metal/metal oxide in addition to the H−UPD current from Pt sites. For example, in Pt−Ru alloy, in addition to hydrogen adsorption on the Pt sites, hydrogen adsorption/absorption occurs in the Ru phase, resulting in a Faradaic current that is the sum of the contributions from Pt and Ru sites. Another method used to determine Pt surface area is CO-stripping voltammetry. This method is also not accurate due to the ambiguity in the adsorption mode of CO on Pt in the presence of the alloyed metals (linear vs bridge bonding), which require different numbers of Pt atoms for adsorption.

Green and Kucernak recently reported the determination of Pt and Ru surface areas in Pt−Ru alloys by the underpotential deposition of copper.[27] In this method, a monolayer of Cu is underpotentially deposited, and from the stripping voltammogram, the surface area can be estimated because the copper stripping reaction is a two-electron-transfer reaction.

$$\underset{\text{(undepotential deposition)}}{Cu^{2+} + 2e^-} \rightarrow Cu_{upd} \rightarrow \underset{\text{(Cu stripping)}}{Cu^{2+} + 2e^-} \qquad (2)$$

For a polycrystalline Pt electrode the charge associated with the above reaction is 420 $\mu C\ cm^{-2}$. We used a similar method to determine the Pt surface area in the Pt−WO_3 catalysts (vide infra).

Results and Discussion

Physical Characterization. *Scanning Electron Microscopy.* Figure 1 shows scanning electron microscopy (SEM) micrographs of the Pt−WO_3 samples obtained at a magnification of 25 000×. The pure Pt sample (S1) consists of spherical particles with particle sizes ranging between 50 and 150 nm. The pure WO_3 sample (S2) shows a surface morphology resembling that of the FTO substrate, indicating the presence of a continuous WO_3 film on top of the substrate rather than isolated particles. For the serially deposited Pt−WO_3 sample (S3), spherical Pt particles are observed on top of the WO_3 film. Samples S4−S9 correspond to the codeposited Pt−WO_3 catalysts. A change in the surface morphology can be clearly observed. When the

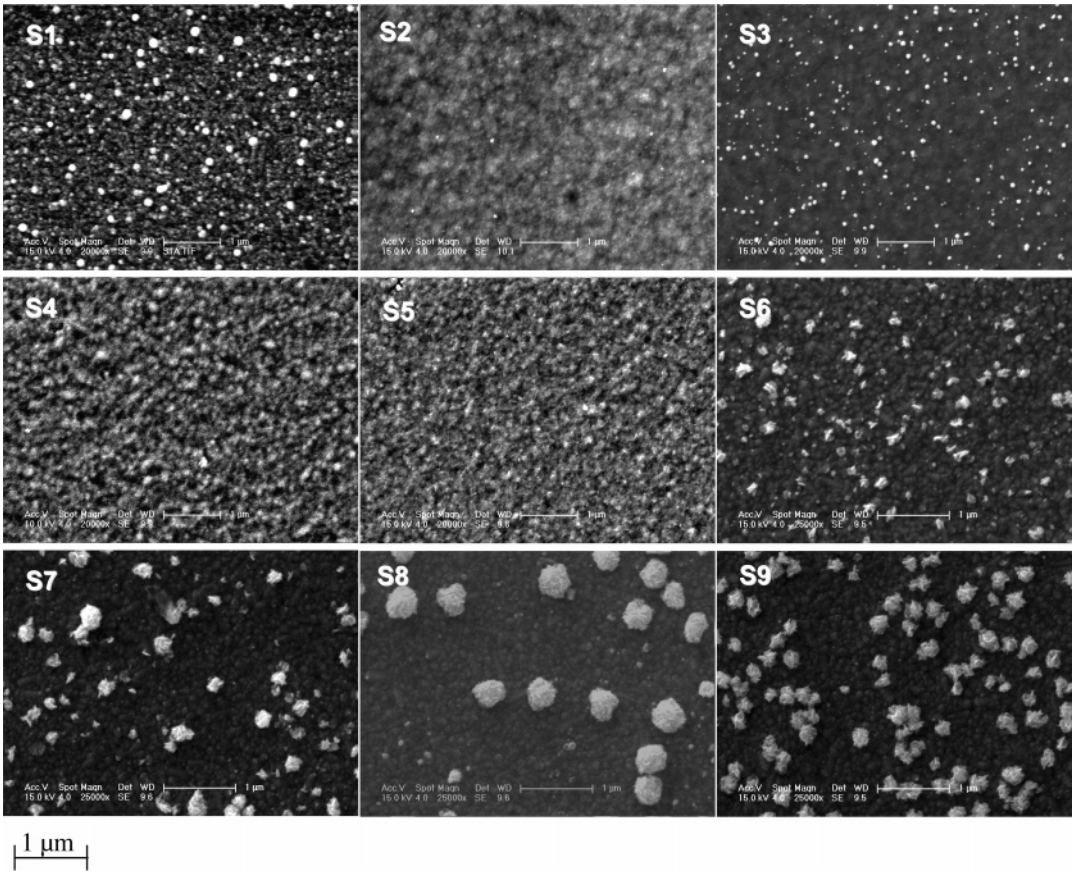

Figure 1. Scanning electron micrographs of Pt−WO_3 samples. The sample numbers correspond to those given in Table 1.

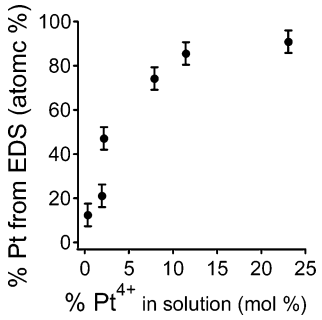

Figure 2. Bulk composition of Pt (from EDS) in the Pt−WO_3 catalysts as a function of Pt^{4+} concentration in the deposition solution.

amount of Pt is increased, the catalyst particles (Pt−WO_3) tend to form clusters. The cluster size increases with increasing Pt composition, peaks at around 85% Pt, and then decreases. In samples S6−S8, the FTO substrate (dark) can be clearly distinguished from the Pt−WO_3 clusters (white). From these results, it is clear that the particle size and structure is influenced by the composition; higher Pt compositions tend to form large, isolated spherical clumps while higher WO_3 compositions tend to form much smaller clumps that link together to produce a fairly flat film morphology that follows the contours of FTO. Although the exact nature of this change is not yet understood, we believe that the evolution in particle structure is an interplay between the deposition of Pt and WO_3 with the surface "wetting" properties induced by the presence of an organic compound such as 2-propanol (which is used to stabilize the peroxo-tungsten electrolyte) in the deposition solution.

X-ray Energy Dispersive Spectroscopy. Figure 2 shows the bulk Pt composition as a function of the concentration of Pt^{4+} ions in the deposition solution of the codeposited films. As expected, an increase in the Pt composition can be observed with increases in the Pt^{4+} concentration (relative to the total ion content of Pt and W). Large amounts of Pt in the catalyst deposit compared to the Pt^{4+} concentration in solution indicate the preferred electrochemical deposition kinetics of Pt compared to that of WO_3. The composition of the serially deposited sample S3, % Pt = 9.58, is not represented in Figure 2. These results indicate that a wide composition range of Pt−WO_3 catalysts has been covered in this study.

Surface Composition: X-ray Photoelectron Spectroscopy. Whereas the EDS provides Pt/W ratios in the bulk of each film, XPS measurements were used to characterize the active surface. Figure 3a exhibits results from high-resolution sweeps of the W 4f spectrum. With the exception of sample S1 (which is pure Pt), all samples exhibit two principal peaks at 36.1 eV (±0.1 eV) and 38.2 eV (±0.1 eV), assigned to the 6+ oxidation state of tungsten for the W $4f_{7/2}$ and W $4f_{5/2}$ spectral lines, respectively.[28] Note that, as expected, the W 4f doublets decrease in intensity progressing from sample S2, which contains no Pt, to sample S9, which contains the greatest fraction of Pt. It is also worthy to note that although the tungsten predominantly exists in a 6+ valence state there also exists a small fraction of W^{5+}, as shown by the small shoulder centered at 35.0 eV for all W-containing samples.[28]

Figure 3b exhibits the Pt 4f spectra for all nine samples. All Pt-containing samples demonstrate similarly asymmetric peaks, indicating multiple oxidation states for Pt. The principal peaks are assigned to Pt^0 at 71.2 eV ($4f_{7/2}$) and 74.5 eV ($4f_{5/2}$).[29] The asymmetry (toward the higher-binding-energy side of these two peaks) arises from the presence of Pt^{2+}, which yields photoemission at 72.3 eV ($4f_{7/2}$) and 75.6 eV ($4f_{5/2}$) (deconvolution not shown).[29] Although most Pt is observed as Pt^0, a significant fraction—approximately 20%—was observed as Pt^{2+} for all Pt-containing samples.

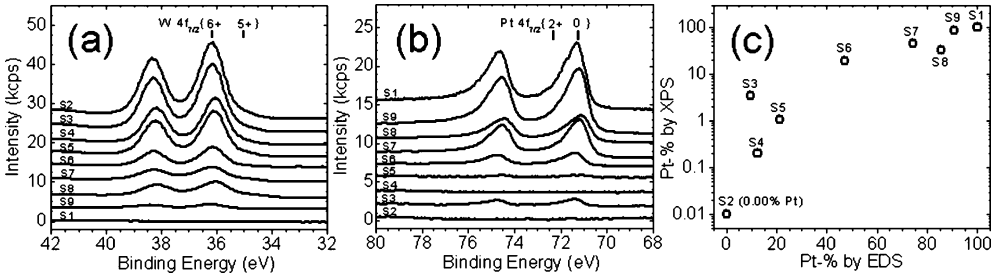

Figure 3. XPS of samples S1−S9. (a) W 4f spectra. (b) Pt 4f spectra. (c) Surface Pt % (by XPS) vs bulk Pt % (by EDS).

Figure 3c compares the fraction of Pt (relative to Pt + W) calculated by XPS (surface) to that determined by EDS (bulk). If Pt and W were homogeneously distributed within each film, then it would be expected that the calculated fractions would be nearly identical by both spectroscopic methods. Our observations are contrary to this expectation; for all samples, it is observed that the surfaces of these films are rich in tungsten and depleted in Pt. The Pt fraction of sample S5, for instance, was measured at approximately 21% by EDS but only 1% by XPS. Sample S7 exhibited 74% Pt by EDS but only 45% by XPS. Although Pt and W are not homogeneously distributed within the films, the trend in Pt % from sample to sample remains the same; i.e., films with greater Pt fractions in the bulk also demonstrated larger Pt fractions at the surface. The two notable exceptions to this trend are samples S3 and S8. It is no surprise that this is the case for sample S3, because this sample was not prepared by co-electro-deposition but rather by serial electro-deposition of Pt on top of an already deposited film of WO_3. Since all of the Pt is at the surface, it is expected that the Pt % determined by XPS for sample S3 should be much higher than that of sample S4 or S5, both of which demonstrated similar overall Pt fractions as S3 (by EDS). The surface fraction of sample S8, however, was lower than expected. We attribute this to the morphology of the sample, because the Pt−WO_3 material formed very large clumps that may hinder Pt photoelectron emission compared to emission from W.

Measurement of Pt Surface Area in Pt−WO_3 Catalysts by Cu Underpoteintal Deposition. Figure 4a shows the Cu-stripping voltammogram of a Pt catalyst deposited on FTO substrate (sample different from S1). A monolayer of Cu was underpotentially deposited, holding the substrate at 0.3 V vs RHE in a solution containing 0.002 M $CuSO_4$/0.1 M H_2SO_4 for 60 s followed by stripping of Cu. The dashed line in the figure shows the background cyclic voltammogram (CV) in 0.1 M H_2SO_4, which was used to estimate the surface area by the H−UPD method. The charges for H−UPD and Cu stripping were determined by integrating the curves in the respective potential regions (0−0.3 V vs RHE for H−UPD and 0.3−0.8 V vs RHE for Cu stripping) and dividing them by the scan rate (0.1 V s^{-1}); the two surface areas were then calculated by dividing the charges associated with these two reactions (210 μC cm^{-2} for H−UPD and 420 μC cm^{-2} for Cu stripping). The Cu-stripping curves were background-subtracted prior to integration; i.e, the current from the CV obtained in 0.1 M H_2SO_4 was subtracted from the Cu-stripping voltammograms for all the samples. The calculated Pt surface areas were 2.085 cm^2 by the H−UPD method and 2.227 cm^2 by the Cu-stripping method, which are in good agreement, indicating the reliability of this method as already shown by Green and Kucernak.[27]

To determine the Pt surface area in a mixed catalyst system such as Pt−WO_3, it is imperative that the method used differentiates Pt and WO_3 sites. The H−UPD method fails for the Pt−WO_3 system due to the intercalation of protons in WO_3,

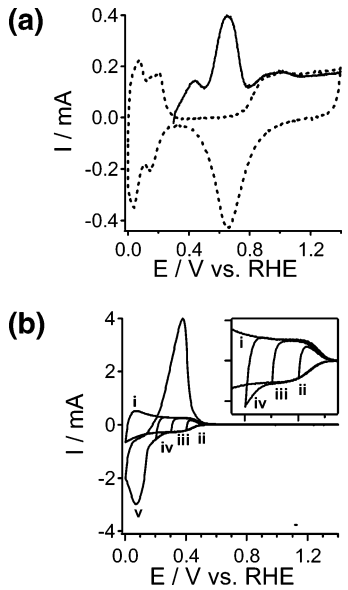

Figure 4. (a) Cu−UPD experiments on polycrystalline Pt. Cyclic voltammogram in 0.1 M H_2SO_4 (dashed line) and Cu-stripping voltammogram (continuous line) of the Pt substrate at a scan rate of 0.1 V s^{-1}. (b) Cu deposition experiments on WO_3 substrate. (i) Cyclic voltammogram of WO_3 substrate in 0.1 M H_2SO_4 at a scan rate of 0.1 V s^{-1}. (ii−v) Cyclic voltammograms of the WO_3 substrate in 0.002 M $CuSO_4$/0.1 M H_2SO_4 at a scan rate of 0.1 V s^{-1} with different potential scan windows. The inset shows an enlarged view of the CVs in the range 0.15−0.5 V.

forming tungsten bronzes[17,23] which occurs in the same potential region (0−0.55 V vs RHE) as H−UPD on Pt. The Cu-stripping method proves to be a viable method for surface area determination in this case. Figure 4b shows the Cu deposition/stripping experiments on a pure WO_3 electrode on FTO substrate. Curve i is the cyclic voltammogram of the electrode in 0.1 M H_2SO_4. Curves ii−v are the cyclic voltammograms of a WO_3 electrode in a solution containing 0.002 M $CuSO_4$/0.1 M H_2SO_4 with increasing cathodic potentials performed in that order. Curves ii and iii overlay exactly on curve i, indicating no underpotential deposition of copper. Curve iv shows the initial stages of bulk Cu deposition, and curve v clearly depicts the bulk Cu deposition and corresponding stripping of bulk Cu. Notably, curve iii shows that at 0.3 V vs RHE—the potential at which underpotential deposition of Cu occurs on Pt—no Cu deposition or stripping current is observed on WO_3. These results clearly indicate that copper underpotential deposition (Cu−UPD) and stripping can be used to estimate the Pt surface area in Pt−WO_3 catalysts.

The Pt surface areas of various Pt−WO_3 samples determined by the Cu-stripping method are presented in Table 1. The currents in all of the electrochemical experiments to follow are normalized to the respective active Pt surface areas.

Electrochemical Characterization. *CVs in Sulfuric Acid.* Cyclic voltammetry of the samples in sulfuric acid provides the background information for the electrochemical processes

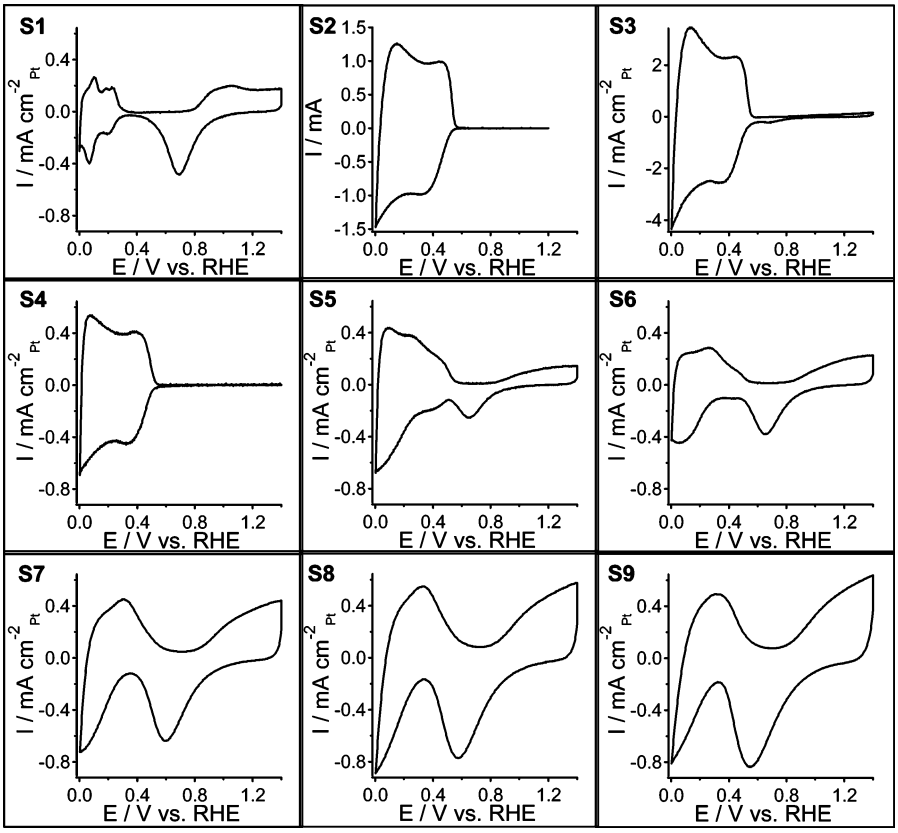

Figure 5. Cyclic voltammograms of Pt−WO_3 samples in 0.5 M H_2SO_4 at a scan rate of 0.1 V s^{-1}.

(Faradaic as well as non-Faradaic) taking place on the catalyst surfaces such as double-layer charging and discharging, hydrogen adsorption and desorption, hydrogen intercalation, formation of surface oxides (M−O_x, M−O_xH_y) and the corresponding reduction of these oxides, etc. Figure 5 depicts the cyclic voltammograms of Pt−WO_3 samples obtained in a solution containing 0.5 M H_2SO_4. The electrochemical currents obtained during the experiments are converted to current densities by normalizing with the corresponding Pt surface area obtained from the Cu−UPD measurements, except sample S2 which is pure WO_3.

Sample S1 (pure Pt) exhibits a typical behavior of polycrystalline Pt with H−UPD adsorption and desorption peaks in the range 0−0.3 V vs RHE, double-layer region between 0.3 and 0.7 V, oxide region beyond 0.8 V, and a corresponding oxide-reduction peak at ∼0.7 V during cathodic scan. In the case of sample S2 (pure WO_3), electrochemical current is observed in the potential region 0−0.55 V vs RHE and is featureless above 0.55 V with zero current. The electrochemical current corresponds to the Faradaic process of intercalation/de-intercalation of H atoms into WO_3, forming tungsten bronzes.[17,23]

$$xH^+ + xe^- + WO_3 \leftrightarrow H_xWO_3 \qquad (3)$$

The well-known electrochromic behavior of WO_3 is observed visually by the colorless WO_3 film turning blue during the cathodic scan and vice versa during the anodic scan. No process other than hydrogen intercalation/de-intercalation takes place on the pure WO_3 substrate within the potential window studied.

The Pt-on-WO_3 sample (S3) exhibits behavior characteristic of both Pt and WO_3. Samples with increasing amounts of Pt (S4−S9) exhibit a more synergistic behavior as opposed to a simple superposition of Pt and WO_3 responses. A clear shift in the onset of the oxide region as well as the oxide-reduction peak can be observed as we traverse from less (12%) to more (91%) Pt (samples S4−S9). Changes in the potential region 0−0.55 V vs RHE can also be observed that seem to result from two simultaneous and different surface phenomena regarding hydrogen adsorption/desorption on Pt and hydrogen intercalation/de-intercalation within WO_3, with the sharpness of the peaks decreasing with increasing Pt contents. Another notable difference between the codeposited Pt−WO_3 catalyst and the pure components is the increase in double-layer charging current.

Methanol Oxidation. Methanol oxidation reaction is a six-electron-transfer reaction, with successive dehydrogenation steps followed by removal of CO.

$$CH_3OH + H_2O \rightarrow CO_2 + 6H^+ + 6e^- \quad E^\circ = 0.03\ V \qquad (4)$$

Figure 6 depicts cyclic voltammograms of the catalyst samples performed in a solution containing 0.5 M CH_3OH/0.5 M H_2SO_4. Only the anodic scans are presented in this figure for the sake of discussion. The pure Pt electrode (S1) shows very low oxidation current at potentials below 0.5 V vs RHE. This low methanol oxidation current is ascribed to the presence of adsorbed CO and other organic intermediates during the initial decomposition of methanol, which prevents the adsorption of hydrogen as well as further adsorption of methanol molecules. The suppression of H−UPD behavior can be clearly observed. At potentials above 0.5 V vs RHE, methanol oxidation commences with an increase in current at anodic potentials with a peak at ∼0.9 V vs RHE.

The response of the WO_3 electrode in methanol/sulfuric acid solution (Figure 6, S2) is exactly the same as that in sulfuric acid without methanol (Figure 5, S2), indicating that WO_3 neither adsorbs methanol nor does it oxidize methanol. The Pt-on-WO_3 sample (S3) shows a curve that seems to be the result of the sum of individual contributions from the WO_3 and

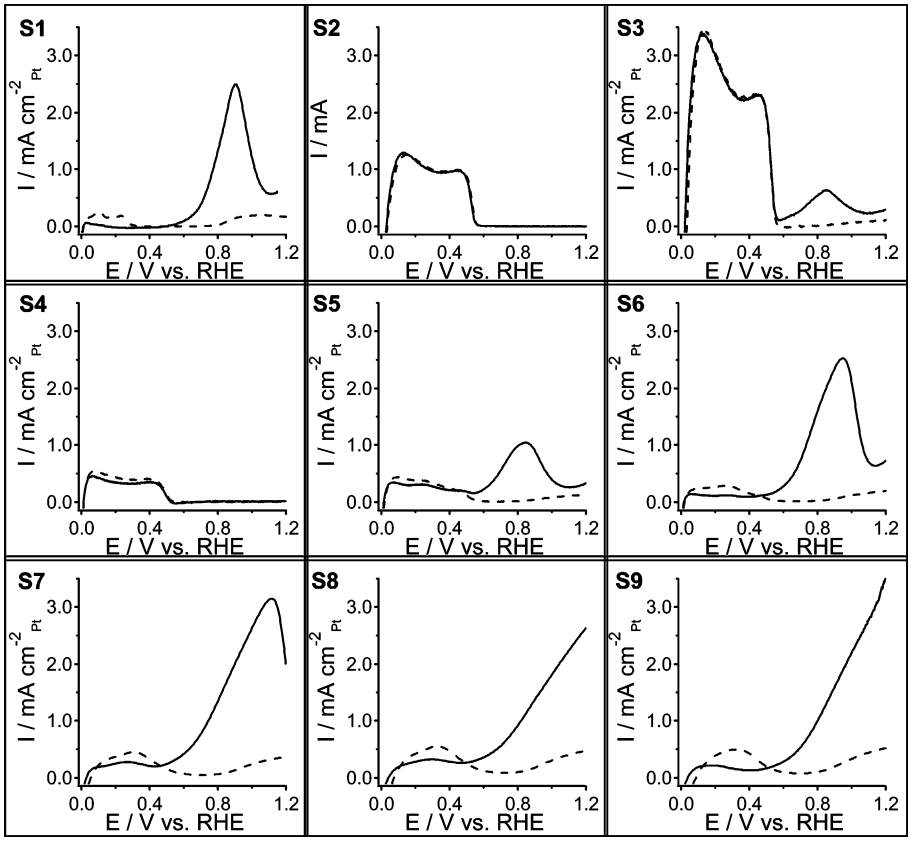

Figure 6. Cyclic voltammograms of Pt−WO_3 samples in 0.5 M CH_3OH/0.5 M H_2SO_4 at a scan rate of 0.1 V s^{-1}. Background CVs in 0.5 M H_2SO_4 are shown as dotted lines.

Pt components. The peak for methanol oxidation in this sample occurs around 0.87 V vs RHE, which is close to that observed for the Pt electrode. However, it has to be noted the current per cm^2 of Pt is much lower compared to that of the pure Pt sample (S1), which we attribute to resistive losses through the WO_3 layer. This may also result from the manner in which Pt deposits on WO_3 compared to the deposition on FTO substrate, which results in the exposure of energetically unfavorable Pt sites with respect to methanol oxidation.

Sample S4 (12% Pt) shows very little current for methanol oxidation (per Pt site) compared to all other Pt-containing samples. This might be due to reasons similar to that of S3 in that energetically unfavorable Pt sites are exposed in addition to charge transport resistance within WO_3. The suppression of current in the H−UPD region can be clearly observed in the rest of the samples (S5−S9 with Pt compositions between 21% and 91%). Also, the methanol oxidation current increases steadily from less to more Pt-containing samples (S5−S9). Another notable feature from these CVs is that the onset of methanol oxidation occurs at potentials much lower than that of Pt, and these currents are significantly higher than that observed for the Pt electrode (S1).

To study the time-dependent behavior of the Pt−WO_3 catalysts toward methanol oxidation, chronoamperometry (CA) experiments were performed. Figure 7 depicts CAs of the Pt−WO_3 electrodes in 0.5 M CH_3OH/0.5 M H_2SO_4 at 0.6 V vs RHE—the onset potential of methanol oxidation on pure Pt—performed for 300 s. All of the samples show steady-state behavior within this time scale. Sample S4 with the least amount of Pt on the surface exhibits very low methanol oxidation current at this potential. Sample S3, which consists of serially deposited Pt on WO_3, is poisoned within a few seconds, and the current goes to zero in a few minutes. Samples S1 (100% Pt) and S5 (21% Pt) show similar behavior to one another with the activity decreasing after several seconds; the current does not drop to zero at the end of the 300 s period. Samples with Pt compositions 47−91% (S6−S9) show higher activity compared to pure Pt (S1). Sample S8 (86% Pt) shows the highest methanol oxidation current (at $t = 300$ s) followed by S7 (74% Pt), S9 (91% Pt), and S6 (47% Pt). The behavior of the Pt−WO_3 samples is consistent with the CVs shown in Figure 6. The higher activity of Pt−WO_3 catalysts at this potential versus Pt indicates an improvement in the poison tolerance and hence an increase in the activity of the catalyst.

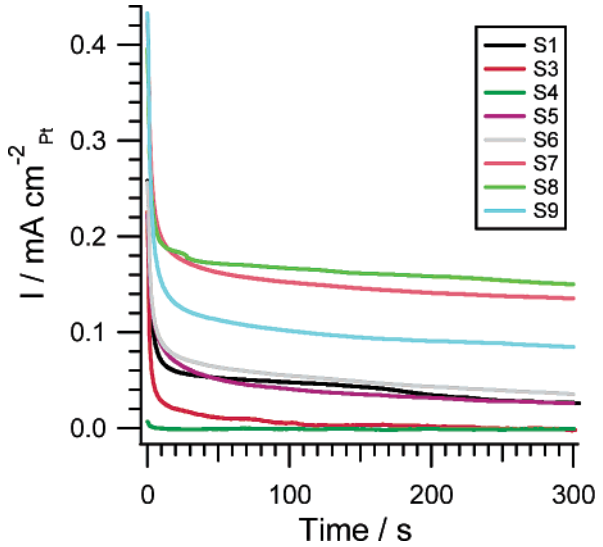

Figure 7. Chronoamperometry (current density vs time) of Pt−WO_3 samples in 0.5 M CH_3OH/0.5 M H_2SO_4 at 0.6 V vs RHE.

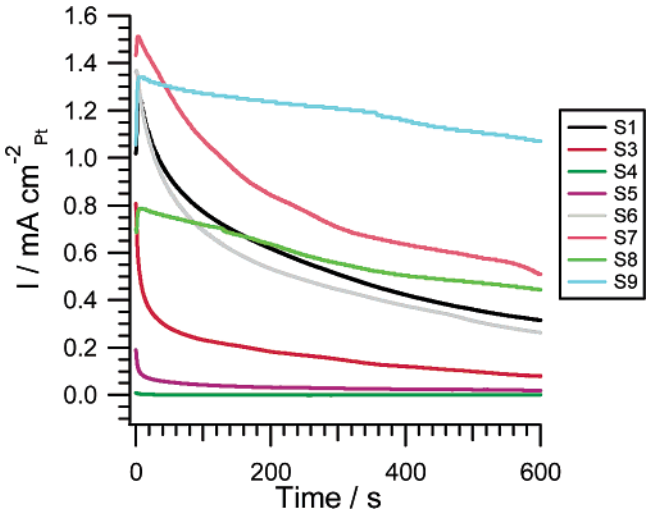

Figure 8. Chronoamperometry (current density vs time) of Pt−WO_3 samples in 0.5 M CH_3OH/0.5 M H_2SO_4 at 0.8 V vs RHE.

Figure 8 shows CAs of the Pt−WO_3 catalysts in 0.5 M CH_3OH/0.5 M H_2SO_4 at 0.8 V vs RHE performed for 600 s. The Pt-on-WO_3 sample (S3) and the samples with 12% (S4) and 21% Pt (S5) show steady-state behavior at the end of 600 s. An increase in the oxidation current, compared to that at 0.6 V vs RHE is observed for all of the samples except S4. This is expected as the onset of surface oxides and hydroxides on Pt occurs at this potential (Figure 5), which enhances the poison-removal processes in addition to increasing the energy supplied to drive the reaction. The sample with 91% Pt (S9) has the highest activity at this potential followed by 74% (S7), 86% (S8), 100% (S1), and 47% (S6) Pt samples.

The improvement in methanol oxidation activity in Pt−WO_3 catalysts is partly attributed to the ability of WO_3 to intercalate H atoms into its matrix, forming tungsten bronzes (eq 3). This feature of WO_3 allows for the spillover of hydrogen from Pt sites into the WO_3 matrix.[19] The dehydrogenation steps in the methanol oxidation reaction are thus facilitated, resulting in a higher turnover on Pt sites. An improvement in the ability to remove CO from the Pt sites is also required to explain the higher activity in Pt−WO_3 catalysts (vide infra), because CO removal is the rate-limiting step of the reaction.

Figure 9 shows the methanol oxidation activity plots for the Pt−WO_3 system as a function of the Pt composition. Figure 9a exhibits the methanol oxidation current density (per cm^2 of Pt) versus % Pt at two different potentials, 0.6 and 0.8 V vs RHE. It is clear from this plot that the current densities measured at 0.8 V are much higher than those at 0.6 V. As discussed earlier, this is due to (1) the onset of surface oxides on Pt at 0.8 V, which facilitate oxidative removal of carbonaceous surface poisons, and (2) the extra 0.2 V supplied to drive the oxidative reaction. From Figure 9a, one can qualitatively observe that Pt−WO_3 catalysts with Pt contents greater than ~50% possess higher activity than pure Pt, both at 0.6 V and at 0.8 V. To quantify this improvement in performance, we constructed Figure 9b, which normalizes the activity of each catalyst versus pure Pt at both 0.6 and 0.8 V.

Although the measured oxidative current densities for Pt−WO_3 catalysts are lower at 0.6 V than those at 0.8V (Figure 9a), Figure 9b demonstrates that at 0.6 V the effects of a mixed catalyst are more pronounced than at 0.8 V. To elucidate this point, let us examine the three top-performing samples: S7 (74% Pt), S8 (85% Pt), and S9 (91% Pt), all of which exhibited greater activity than pure Pt. At 0.8 V, these three catalysts exhibited

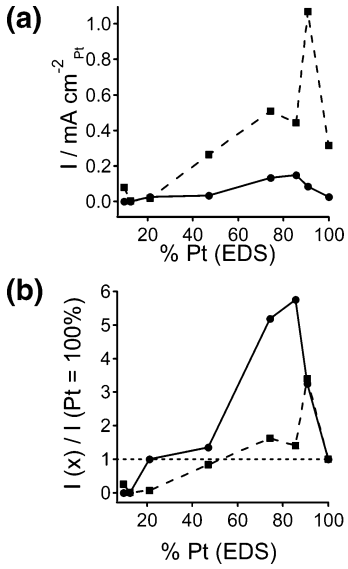

Figure 9. Methanol oxidation activity plots for the Pt−WO_3 catalyst system as a function of Pt composition at two different substrate potentials of 0.6 V vs RHE (continuous line and circles) and 0.8 V vs RHE (dashed line and squares). (a) Current density at 300 s for 0.6 V data and at 600 s for 0.8 V data as a function of the Pt composition. (b) Normalized current density as a function of Pt composition. The curves were obtained by dividing the current density of each of the samples at 300 s for 0.6 V data and at 600 s for 0.8 V data with that of the corresponding current density of the 100% Pt sample (S1).

1.6×, 1.4×, and 3.4× greater performance than pure Pt, respectively. At 0.6 V, the same catalysts exhibited 5.2×, 5.8×, and 3.2× improvements, respectively, over pure Pt. The normalized results suggest that at 0.6 V the presence of WO_3 is even more critical because surface oxides on Pt are not formed at this potential, unlike the case at 0.8 V. From a practical point of view, in a fuel cell for a given power output one can utilize Figure 9b to determine the optimal Pt loading for the Pt−WO_3 catalyst system. If operation of the cell at a higher cell potential (i.e., at a lower anodic overpotential) is desired, then Figure 9b shows that the Pt loading can be decreased to a much lower value by employing the Pt−WO_3 catalysts—achieving nearly a 6-fold improvement over pure Pt—which results in lower fuel cell cost for a given power output.

CO-Stripping Voltammetry. The poison tolerance of the Pt−WO_3 catalysts toward CO was tested by CO-stripping voltammetry. CO was adsorbed by holding the substrate at 0.05 V vs RHE in a CO-saturated solution of 0.5 M H_2SO_4 for 20 min. This was followed by removal of CO from the solution by purging N_2 for 20 min while still holding the substrate at this potential. CVs were obtained subsequently at a scan rate of 0.1 V s^{-1}. Figure 10 shows CO-stripping voltammograms of the Pt−WO_3 catalysts. Sample S1 exhibits typical CO-oxidation behavior on a Pt electrode with a peak at ~0.75 V and a shoulder (known as a "prewave") at ~0.55 V. The prewave corresponds to the removal of linearly bonded CO, and the main peak corresponds to the removal of bridge-bonded CO. The potentials at which CO oxidation occurs correspond to that of water dissociation, which forms surface oxides responsible for the oxidative removal of CO.

$$\mathrm{Pt{-}CO_{ads}} + \mathrm{Pt{-}OH_{ads}} \rightarrow \mathrm{Pt} + \mathrm{CO_2} + \mathrm{H^+} + \mathrm{e^-} \quad (5)$$

The pure WO_3 sample (Figure 10, S2) shows a behavior different from that shown in Figure 5. An additional peak at ~0.25 V vs RHE is observed in addition to the broad H de-

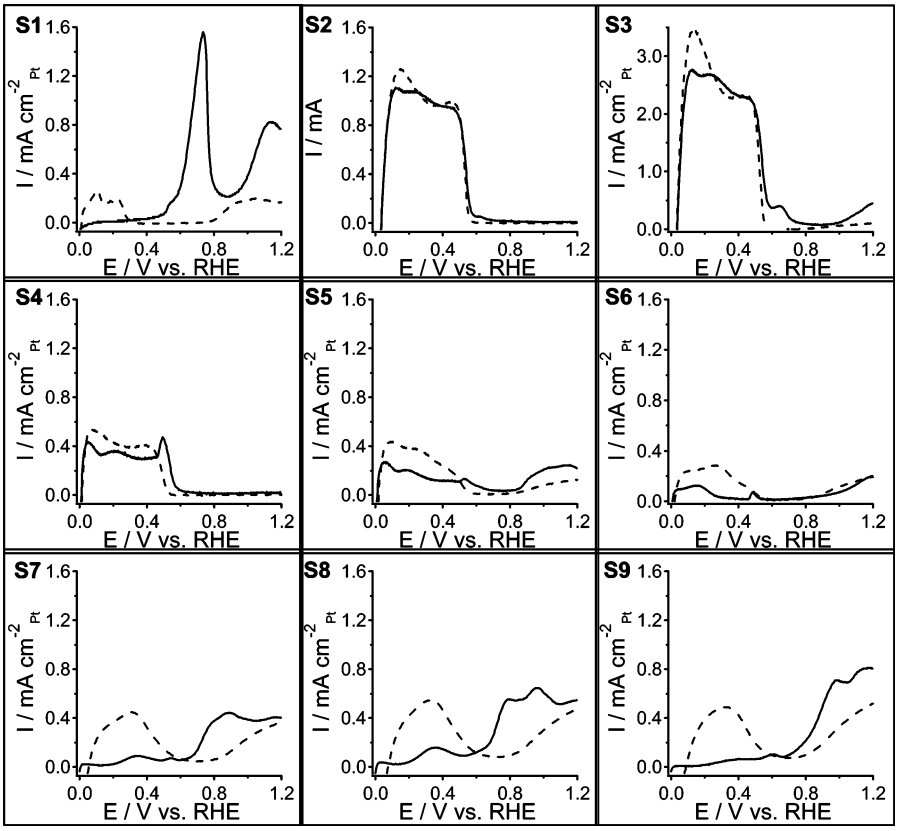

Figure 10. CO-stripping voltammetry of Pt−WO_3 electrodes in a nitrogen-purged solution of 0.5 M H_2SO_4 at a scan rate of 0.1 V s^{-1}. The background CVs in 0.5 M H_2SO_4 are shown as dashed lines.

intercalation peaks. This is possibly due to the oxidation of CO by WO_3. A small shoulder can also be observed at ~0.6 V. The oxidation peak at ~0.25 V appears in all of the Pt−WO_3 samples, with the peak position shifting to slightly more anodic values (to ~0.3 V) with increasing Pt composition. Although the exact mechanism of CO oxidation on WO_3 needs further analysis, we speculate that tungsten changes oxidation states between +6 and +5 in this potential region, providing the oxygen species required for the removal of CO. The XPS results, which were obtained ex situ, show the presence of small amounts of W^{5+} in addition to W^{6+}. This result is in contrast with that observed with chemically synthesized Pt−WO_3 catalysts[25] in which the authors report that the enhancement in catalytic activity is mainly due to some "physical" modification of Pt such as surface area rather than mechanistic improvements in the surface catalysis. To study the catalytic enhancement more rigorously, we are planning more detailed XPS studies as well as in situ IR studies.

Conclusions

Pt−WO_3 catalysts were electrochemically synthesized with a wide range of compositions, and their activity toward the methanol oxidation reaction was investigated. The Pt-specific surface area was determined by the Cu−UPD method, which is sensitive to Pt sites but not to the surrounding WO_3 matrix. A performance relationship for methanol oxidation was constructed based on the electrochemical activity as a function of Pt composition in the catalysts. From this graph, appropriate catalyst compositions can be selected for a given fuel cell system to minimize the Pt loading. In general, catalysts with Pt compositions greater than 50% showed higher activity compared to pure Pt, with a few compositions showing improvements as high as 5.8×. A mechanism for poison tolerance is also proposed in which WO_3 takes part in removal CO in addition to abstracting protons, resulting in an improved overall performance of Pt−WO_3 catalysts for methanol oxidation.

Acknowledgment. The authors thank Mr. Jose Saleta of the Donald Bren School of Environmental Science and Management, University of California, Santa Barbara, for the help with SEM−EDS measurements and Alan Kleiman-Shwarsctein for the help with software development.

Supporting Information Available: Cu−UPD experiments on the Pt−WO_3 catalyst samples and a cyclic voltammogram of the FTO substrate in 0.002 M $CuSO_4$/0.1 M H_2SO_4 at a scan rate of 0.1 V s^{-1}. This material is available free of charge via the Internet at http://pubs.acs.org.

References and Notes

(1) Scott, K.; Taama, W. M.; Argyropoulos, P. *J. Power Sources* **1999**, *79*, 43.
(2) Baxter, S. F.; Battaglia, V. S.; White, R. E. *J. Electrochem. Soc.* **1999**, *146*, 437.
(3) Kelley, S. C.; Deluga, G. A.; Smyrl, W. H. *Electrochem. Solid-State Lett.* **2000**, *3*, 407.
(4) Lamy, C.; Lima, A.; LeRhun, V.; Delime, F.; Coutanceau, C.; Leger, J. M. *J. Power Sources* **2002**, *105*, 283.
(5) Li, Q. F.; Hjuler, H. A.; Hasiotis, C.; Kallitsis, J. K.; Kontoyannis, C. G.; Bjerrum, N. J. *Electrochem. Solid-State Lett.* **2002**, *5*, A125.
(6) McNicol, B. D.; Rand, D. A. J.; Williams, K. R. *J. Power Sources* **1999**, *83*, 15.
(7) Jayaraman, S.; Hillier, A. C. *J. Phys. Chem. B* **2003**, *107*, 5221.
(8) Jayaraman, S.; Hillier, A. C. *J. Comb. Chem.* **2004**, *6*, 27.
(9) Arico, A. S.; Antonucci, V.; Giordano, N.; Shukla, A. K.; Ravikumar, M. K.; Roy, A.; Barman, S. R.; Sarma, D. D. *J. Power Sources* **1994**, *50*, 295.
(10) Beden, B.; Kadirgan, F.; Lamy, C.; Leger, J. M. *J. Electroanal. Chem.* **1981**, *127*, 75.
(11) Choi, W. C.; Kim, J. D.; Woo, S. I. *Catal. Today* **2002**, *74*, 235.

(12) Chrzanowski, W.; Wieckowski, A. *Langmuir* **1998**, *14*, 1967.
(13) Crown, A.; Moraes, I. R.; Wieckowski, A. *J. Electroanal. Chem.* **2001**, *500*, 333.
(14) Gurau, B.; Viswanathan, R.; Liu, R. X.; Lafrenz, T. J.; Ley, K. L.; Smotkin, E. S.; Reddington, E.; Sapienza, A.; Chan, B. C.; Mallouk, T. E.; Sarangapani, S. *J. Phys. Chem. B* **1998**, *102*, 9997.
(15) Jayaraman, S.; Hillier, A. C. *Meas. Sci. Technol.* **2005**, *16*, 5.
(16) Reddington, E.; Sapienza, A.; Gurau, B.; Viswanathan, R.; Sarangapani, S.; Smotkin, E. S.; Mallouk, T. E. *Science* **1998**, *280*, 1735.
(17) Baeck, S. H.; Jaramillo, T. F.; McFarland, E. W. *Abstracts of Papers*, 224th National Meeting of the American Chemical Society; American Chemical Society: Washington, DC, 2002; U565.
(18) Baeck, S. H.; Jaramillo, T. F.; Stucky, G. D.; McFarland, E. W. *Nano Lett.* **2002**, *2*, 831.
(19) Park, K.-W.; Ahn, K.-S.; Nah, Y.-C.; Choi, J.-H.; Sung, Y.-E. *J. Phys. Chem. B* **2003**, *107*, 4352.
(20) Shen, P. K.; Tseung, A. C. C. *J. Electrochem. Soc.* **1994**, *141*, 3082.
(21) Shen, P.; Chen, K.; Tseung, A. C. C. *J. Chem. Soc., Faraday Trans.* **1994**, *90*, 3089.
(22) Shukla, A. K.; Ravikumar, M. K.; Arico, A. S.; Candiano, G.; Antonucci, V.; Giordano, N.; Hamnett, A. *J. Appl. Electrochem.* **1995**, *25*, 528.
(23) Su, L.; Zhang, L.; Fang, J.; Xu, M.; Lu, Z. *Solar Energy Mater. Solar Cells* **1999**, *58*, 133.
(24) Umeda, M.; Ojima, H.; Mohamedi, M.; Uchida, I. *J. Power Sources* **2004**, *136*, 10.
(25) Yang, L. X.; Bock, C.; MacDougall, B.; Park, J. *J. Appl. Electrochem.* **2004**, *34*, 427.
(26) Scofield, J. H. *J. Electron Spectrosc. Relat.Phenom.* **1976**, *8*, 129.
(27) Green, C. L.; Kucernak, A. *J. Phys. Chem. B* **2002**, *106*, 1036.
(28) Stolze, M.; Camin, B.; Galbert, F.; Reinholz, U.; Thomas, L. K. *Thin Solid Films* **2002**, *409*, 254.
(29) Zhang, X.; Kwong-yu, C. *Chem. Mater.* **2003**, *15*, 451.